JOURNAL OF GUIDANCE, CONTROL, AND DYNAMICS
Vol. 17, No. 4, July–August 1994

Multiaxis Tracking and Attitude Control of Flexible Spacecraft with Reaction Jets

Hari B. Hablani*
Rockwell International, Seal Beach, California 90740

The objective of this paper is to show that integral pulse frequency modulation (IPFM) reaction jet controllers can perform, with precision: multiaxis tracking of moving objects, attitude control of flexible spacecraft under orbit-adjustment forces, single-axis slews, and vibration suppression. Two sets of position, rate, and acceleration command profiles for multiaxis tracking are presented: one for a payload initially facing the zenith and the commands based on a pitch-roll sequence; the other for a payload facing the nadir and the commands based on a roll-pitch sequence. The procedure for designing an IPFM controller for tracking a given, inertial acceleration command profile is summarized. Important elastic modes of a spacecraft are identified according to their spontaneous attitude and rate response to the minimum impulse bit of the thrusters. The stability of control-structure interaction is shown to be governed by the ratio of the moments of inertia of the flexible to the rigid portions of the spacecraft. If this ratio is below unity for each axis, the spacecraft is stable; otherwise it is not. The stability inequality for symmetric elastic modes, when they induce attitude motion because of a moment arm from the vehicle mass center, is formulated. Extensive numerical results conclusively establish that the IPFM controllers are eminently suitable for the tasks mentioned above.

I. Introduction

THIS paper presents novel applications of integral pulse frequency modulation (IPFM) reaction jet control systems for flexible, precision pointing spacecraft; the applications are multiaxis tracking of moving objects, spacecraft attitude control under station-keeping or orbit-adjustment forces, single-axis slews, and vibration suppression to minimize jitter. The contents of the paper and the pertinent literature are reviewed below briefly.

Section II of the paper, following Ref. 1, develops multiaxis position, rate, and acceleration command profiles for tracking a moving object. The position commands involve Euler angles, and the rate and acceleration commands are inertial, expressed about the spacecraft axes. The following two possible scenarios are considered: a payload rigidly attached to the spacecraft bus, facing the zenith initially, and tracking commands based on a pitch-roll sequence; and the payload facing the nadir initially and the commands based on a roll-pitch sequence. These commands are used as reference trajectories to determine the position and rate errors for the IPFM reaction jet controllers. Farrenkopf et al.[2] presented a complete procedure for designing this controller, and compared its performance with a saturating proportional-plus-derivative controller and a relay controller with a deadband and hysteresis. Abdel-Rahman[3] compared it further with a dual time constant pseudorate controller. The unique characteristics and benefits of an IPFM controller are that it activates a thruster pulse of constant width whenever the integral of a linear combination of position and rate errors exceeds a certain threshold; the frequency of the jet firing is thereby modulated, keeping the pulsewidth constant. Farrenkopf et al.[2] conclude that because of integration of the errors, the effect of sensor noise is mitigated considerably and the attitude control is much smoother by an IPFM controller than by a pseudorate controller. This is true also because of availability of the rate error. Owing to these features, the IPFM controller is not as debilitated by structural flexibility as a pseudorate controller is, even when the natural damping of the structure is low ($\zeta \approx 0.0025$) and the sensor time lag large.[3] For these reasons, the IPFM controllers are employed here for target tracking which requires large-angle multiaxis attitude motions, and for spacecraft attitude control under disturbance torques. Section III of the paper summarizes the relationships for determining the control parameters for these tasks, and describes a multiaxis tracking controller.

Thrusters are particularly prone to exciting flexible modes of a spacecraft. To examine this interaction, we present scalar metrics in Sec. IV to identify important modes from infinite of them. The interaction between nonlinear reaction jet controllers and structures has been analyzed in the past using describing function and Lyapunov techniques; see, for example, Refs. 4–6 for the former and Ref. 3 for the latter. These analyses tend to be rather sophisticated, however; so, by way of contrast, we furnish in Sec. IV simple but intuitive criteria of stability involving the ratio of the moments of inertia of the flexible to the rigid portions I_f/I_r of the spacecraft about each of the three axes. Next, when symmetric elastic modes interact with spacecraft attitude owing to their moment arm from the vehicle mass center, thrusters must be located carefully because their translational force is not of the same genre as the angle measured by an IMU gyro. The corresponding linear stability conditions for thrusters are derived in Sec. IV following Gevarter.[7] Moreover, even if this linear stability condition is satisfied, unstable control-structure interaction becomes inevitable when a certain axis of the spacecraft is very flexible ($I_f/I_r \gg 1$) unless filters—a double notch filter (Blakelock[8]), for example—are incorporated in the controller. See Wie and Plescia[5] for an example of this instability for $I_f/I_r \approx 5.8$. An alternative to these filters, namely, a minimum-rise-time, low-pass filter is considered in the conference version of this paper.[9] Finally, Sec. V of the paper illustrates multiaxis tracking and attitude control under disturbances, and the paper is concluded in Sec. VI.

II. Command Profiles for Tracking a Moving Target

Position Commands

Figure 1 illustrates relative locations of the Earth, a spacecraft in a circular orbit, and a moving target to be tracked. The

Received Sept. 18, 1992; revision received Sept. 20, 1993; accepted for publication Sept. 21, 1993.

*Senior Engineering Specialist, Guidance and Control Group, Space Systems Division. Senior Member AIAA.

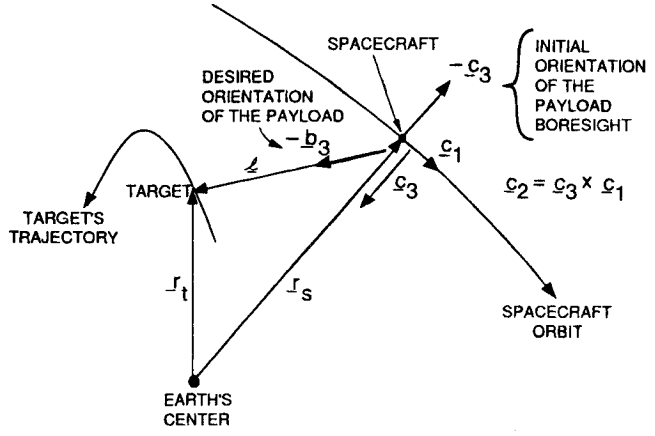

Fig. 1 Earth, spacecraft, and target to be tracked.

spacecraft's orbit and the target's trajectory are both taken to be known. Measured from the Earth's mass center, the spacecraft is at a location $\boldsymbol{r}_s$ and the target at $\boldsymbol{r}_t$. The ideal line-of-sight (LOS) vector $\boldsymbol{\ell}$ is $\boldsymbol{\ell} = -\boldsymbol{r}_s + \boldsymbol{r}_t$. Ideally, this vector must be along the payload boresight, which is assumed to be along the negative yaw axis ($-\boldsymbol{b}_3$ unit vector, $\boldsymbol{b}$ for body). Before acquiring the target, the spacecraft-fixed triad ($\boldsymbol{b}_1, \boldsymbol{b}_2, \boldsymbol{b}_3$) is aligned with the local-vertical-local-horizontal unit vector triad $\boldsymbol{c}_1, \boldsymbol{c}_2, \boldsymbol{c}_3$ (shown in Fig. 1), implying that, initially, the payload boresight is along $-\boldsymbol{c}_3$ (facing the zenith). Because the vectors $\boldsymbol{r}_s$ and $\boldsymbol{r}_t$ are known in the geocentric inertial frame, the LOS vector $\boldsymbol{\ell}$ can be calculated, after coordinate transformations, in the orbital triad $\boldsymbol{c}_1$, $\boldsymbol{c}_2$, $\boldsymbol{c}_3$ and expressed as

$$\boldsymbol{\ell} = \boldsymbol{\ell} \cdot \boldsymbol{c}_1 \boldsymbol{c}_1 + \boldsymbol{\ell} \cdot \boldsymbol{c}_2 \boldsymbol{c}_2 + \boldsymbol{\ell} \cdot \boldsymbol{c}_3 \boldsymbol{c}_3 \tag{1}$$

To bring the target to the focal plane center of the payload, the spacecraft is rotated about the vector $\boldsymbol{c}_2$ by an angle θ_{yc} and then about the displaced axis $\boldsymbol{c}_1$ by an angle θ_{xc}. Following Ref. 1, these angular commands can be shown to be

$$\theta_{yc} = \tan^{-1}\left[-\boldsymbol{\ell} \cdot \boldsymbol{c}_1 / -\boldsymbol{\ell} \cdot \boldsymbol{c}_3\right] \tag{2a}$$

$$\theta_{xc} = \sin^{-1}\left[\boldsymbol{\ell} \cdot \boldsymbol{c}_2 / \ell\right] \tag{2b}$$

where $\ell \triangleq |\boldsymbol{\ell}|$. The negative signs in the numerator and the denominator in Eq. (2a) are retained so as to identify the correct quadrant of the pitch command θ_{yc}; the roll command θ_{xc} will always be $-\pi/2 \leq \theta_{xc} \leq \pi/2$. In Ref. 9, these commands are simplified for landmarks on the rotating Earth. The commanded yaw angle, θ_{zc}, is zero and so is its rate $\dot{\theta}_{zc}$; this does not mean, however, that the yaw (z-) component ω_{zc} of the commanded inertial rate $\boldsymbol{\omega}_c$ is zero. The commanded roll, pitch and yaw inertial rate components (ω_{xc}, ω_{yc}, ω_{zc}) of ω_c are derived below.

Rate and Acceleration Commands

The inertial LOS-rate $\dot{\boldsymbol{\ell}}$ (an overdot implies inertial differentiation) is calculated from $\dot{\boldsymbol{\ell}} = -\dot{\boldsymbol{r}}_s + \dot{\boldsymbol{r}}_t$, which can be transformed readily from the geocentric inertial frame to the orbit frame $\boldsymbol{c}_1$, $\boldsymbol{c}_2$, $\boldsymbol{c}_3$. Knowing the position command angles from the preceding, $\dot{\boldsymbol{\ell}}$ can then be expressed in the desired orientation of the body frame $\boldsymbol{b}_1$, $\boldsymbol{b}_2$, $\boldsymbol{b}_3$. Also, the allowable change in $\boldsymbol{\ell}$ in the body frame is $\mathring{\boldsymbol{\ell}} = -\dot{\boldsymbol{\ell}}\, \boldsymbol{b}_3$ where an overcircle denotes the differentiation in a rotating frame. Following Ref. 1 again, the inertial roll and pitch rate commands ω_{xc} and ω_{yc}, respectively, are found to be

$$\omega_{xc} = \dot{\boldsymbol{\ell}} \cdot \boldsymbol{b}_2 / \ell \tag{3a}$$

$$\omega_{yc} = -\dot{\boldsymbol{\ell}} \cdot \boldsymbol{b}_1 / \ell \tag{3b}$$

and the rate of change $\mathring{\ell}$ is: $\mathring{\ell} = -\dot{\boldsymbol{\ell}} \cdot \boldsymbol{b}_3$. Next, to determine the yaw component ω_{zc}, we recognize that, in all, the spacecraft has three desired angular rates: the clockwise rotation $-\omega_0 \boldsymbol{c}_2$ for Earth-pointing, the pitch rate command $\dot{\theta}_{yc}\, \boldsymbol{c}_2$, and the roll rate command $\dot{\theta}_{xc}\, \boldsymbol{b}_1$. The total inertial rate command $\boldsymbol{\omega}_c$ is therefore

$$\begin{aligned}\boldsymbol{\omega}_c &= [\omega_{xc}\ \omega_{yc}\ \omega_{zc}]^T \\ &= [\dot{\theta}_{xc}\ (\dot{\theta}_{yc} - \omega_0)\ c\theta_{xc} - (\dot{\theta}_{yc} - \omega_0)\ s\theta_{xc}]^T\end{aligned} \tag{4}$$

where $c(\cdot) = \cos(\cdot)$ and $s(\cdot) = \sin(\cdot)$. The second and third elements of Eq. (4) yield

$$\omega_{zc} = -\omega_{yc} \tan \theta_{xc} \tag{5}$$

Thus, the inertial yaw rate w_{zc} is not a second-order quantity even for a small roll angle θ_{xc}.

The acceleration commands are eminently useful for feedforward and/or for determining the inertial resistance the spacecraft will put forth in tracking a moving target. The derivation of these commands parallels the development in Ref. 1 and we arrive at

$$\dot{\omega}_{xc} = (\ddot{\boldsymbol{\ell}} \cdot \boldsymbol{b}_2 - 2\, \mathring{\ell}\, \omega_{xc}) / \ell + \omega_{yc}\, \omega_{zc} \tag{6}$$

$$\dot{\omega}_{yc} = -(\ddot{\boldsymbol{\ell}} \cdot \boldsymbol{b}_1 + 2\, \mathring{\ell}\, \omega_{yc}) / \ell - \omega_{xc}\, \omega_{zc} \tag{7}$$

where the inertial acceleration $\ddot{\boldsymbol{\ell}}$ of LOS $\boldsymbol{\ell}$ equals $(-\ddot{\boldsymbol{r}}_s + \ddot{\boldsymbol{r}}_t)$. The inertial yaw acceleration command $\dot{\omega}_{zc}$ is derived by differentiating Eq. (5) and recognizing that, for the pitch-roll sequence, $\omega_{xc} = \dot{\theta}_{xc}$. We then arrive at

$$\dot{\omega}_{zc} = -\dot{\omega}_{yc} \tan \theta_{xc} - \omega_{xc}\, \omega_{yc} \sec^2 \theta_{xc} \tag{8}$$

From the commands (5) and (8) we see that, although θ_{zc} and $\dot{\theta}_{zc}$ are both zero, ω_{zc} and $\dot{\omega}_{zc}$ are not. [Eq. (15c), Ref. 9, is incorrect, as it does not contain the second term in the right side of Eq. (8) of this paper.]

While the preceding pointing commands are based on a pitch-roll sequence and are for a payload initially facing the zenith, Table 1 furnishes the commands using a roll-pitch Euler angle sequence for a payload facing the nadir initially. The rate and acceleration commands ω_{zc} and $\dot{\omega}_{zc}$ in Table 1 are lengthier than their counterpart, commands (5) and (8) because, for the roll-pitch sequence, the orbit rate ω_0 about $\boldsymbol{c}_2$ cannot be expressed as simply about the pitch axis $\boldsymbol{b}_2$ as it can be for the pitch-roll sequence. Both sequences are useful nonetheless, because when one is singular the other is not.

The conditions of visibility of the target from the spacecraft are covered in detail in Ref. 9.

Table 1 Pointing commands for tracking a moving object: payload boresight initially facing nadir and roll-pitch sequence

Attitude commands	$\theta_{xc} = \tan^{-1}(-\boldsymbol{\ell} \cdot \boldsymbol{c}_2)/(\boldsymbol{\ell} \cdot \boldsymbol{c}_3)$, $\theta_{yc} = \sin^{-1}(\boldsymbol{\ell} \cdot \boldsymbol{c}_1/\ell)$
Inertial rate commands	$\omega_{xc} = -\dot{\boldsymbol{\ell}} \cdot \boldsymbol{b}_2 / \ell$, $\omega_{yc} = \dot{\boldsymbol{\ell}} \cdot \boldsymbol{b}_1 / \ell$ $\omega_{zc} = \omega_0\, s\theta_{xc} / c\theta_{yc} + \omega_{xc} \tan \theta_{yc}$
Inertial acceleration commands	$\dot{\omega}_{xc} = -(\ddot{\boldsymbol{\ell}} \cdot \boldsymbol{b}_2 + 2\, \mathring{\ell}\, \omega_{xc}) / \ell + \omega_{yc}\, \omega_{zc}$ $\dot{\omega}_{yc} = (\ddot{\boldsymbol{\ell}} \cdot \boldsymbol{b}_1 - 2\, \mathring{\ell}\, \omega_{yc}) / \ell - \omega_{xc}\, \omega_{zc}$ $\dot{\omega}_{zc} = \omega_0\, (\dot{\theta}_{xc}\, c\theta_{xc}\, c\theta_{yc} + \dot{\theta}_{yc}\, s\theta_{xc}\, s\theta_{yc}) \sec^2 \theta_{yc} + \omega_{xc}\, \dot{\theta}_{yc} \sec^2 \theta_{yc} + \dot{\omega}_{xc} \tan \theta_{yc}$
where	$\mathring{\ell} = \dot{\boldsymbol{\ell}} \cdot \boldsymbol{b}_3$ $\dot{\theta}_{xc} = (\omega_{xc} + \omega_0\, s\theta_{xc}\, s\theta_{yc}) \sec \theta_{yc}$ $\dot{\theta}_{yc} = \omega_{yc} + \omega_0\, c\theta_{xc}$

III. Integral Pulse Frequency Modulation Reaction Jet Controller

Single-Axis Mode of Operation

A single-axis IPFM reaction jet controller—a modified version of the one considered in Refs. 2, 3, and 10—is shown in Fig. 2. Bernussou[10] formulates a varying integral threshold, called A_I in Fig. 2, to keep the attitude error extrema nearly the same whether external disturbances are present or not; A_I is constant in this study, however. The special features of the IPFM controller in Fig. 2 are: timevarying position and rate commands Θ_c and $\dot{\Theta}_c$, [Because of flexible modes, an angle based on rigid body analysis is denoted Θ, while the total angle is denoted θ], a rate gyro to measure the spacecraft rate $\dot{\theta}$, and a structural filter to strain out excited flexible modes from noisy gyro signal $\dot{\theta}_n$ if the axis under consideration is overly flexible. When the IPFM controller is used to slew the spacecraft or acquire a moving target, the commands Θ_c and $\dot{\Theta}_c$ may be the reference trajectories developed in Refs. 11 or 12, and when a target is to be tracked, the position and rate commands of Sec. II are used. Moreover, for attitude hold, both Θ_c and $\dot{\Theta}_c$ will be zero. An IMU gyro is included in Fig. 2 instead of an attitude sensor and a lead-lag compensation (as in Refs. 2, 3, and 10) because precise attitude and rate measurements facilitate a smooth control of attitude as well as jitter caused by elastic modes (See Sec. V). Very briefly, the IPFM controller functions as follows.

The spacecraft attitude θ and the rate $\dot{\theta}$ consist of rigid and elastic modes, as shown in Fig. 2. The rigid attitude is denoted Θ, and the attitude angle contributed by μth vehicle elastic mode θ_μ, where $\theta_\mu(t) = \Phi_\mu \eta_\mu(t)$, Φ_μ equals the μth rotational modal coefficient at the sensor location, and $\eta_\mu(t)$ is the μth modal coordinate. Mathematically,

$$\theta(t) = \Theta(t) + \sum_{\mu=1}^{\infty} \theta_\mu(t) = \Theta(t) + \sum_{\mu=1}^{\infty} \Phi_\mu \eta_\mu(t) \qquad (9)$$

The attitude rate counterpart of Eq. (9) passes through the IMU gyro of bandwidth ω_g, giving rise to a noise-free output $\dot{\theta}_g$, which, when blended with gyro noise n_g, becomes the noisy attitude rate $\dot{\theta}_n$. The gyro output $\dot{\theta}_n$ is passed through a structural filter if necessary, yielding thereby $\dot{\theta}_{nf}$, a quantity very similar but not identical to the rigid rate $\dot{\Theta}$. When the axis under consideration is moderately flexible, this filter is not used, and $\dot{\theta}_{nf} = \dot{\theta}_n$. Knowing the command profiles Θ_c and $\dot{\Theta}_c$, the position and rate errors are calculated as shown, and a composite error signal e equal to $(\theta_e + K_d \dot{\theta}_e)$ is formed, and its integral e_I ($\dot{e}_I = e$) is compared with the threshold $\pm A_I$ at a desired sampling frequency. When $|e_I| \geq A_I$, the thrusters are fired for a constant pulsewidth τ_w, with the polarity of the control torque T_c determined by sgn T_c = sgn e_I. As soon as the thrusters are turned on, the integral e_I is reset to zero and the integration of the error signal e commences afresh (with the initial condition $e_I = 0$). The integration proceeds even while the thrusters are on to ensure that, if necessary, the thrusters will be saturated. The control torque T_c and the disturbance torque T_d act on the spacecraft, producing the attitude rate $\dot{\theta}$, and the preceding operation recurs in a closed-loop fashion.

To determine the control parameters appearing previously, we observe that a reaction jet controller is required to counteract disturbances such as those caused by station-keeping or orbit-adjustment forces which produce a torque when the resultant force does not pass through the vehicle mass center. Analogously, when a spacecraft is slewed or commanded to track a target, the controller confronts inertial resistance of the spacecraft equal to the central, principle moment of inertia I_V times the desired acceleration. The controller then must prevail against the extreme inertial resistance and slew the spacecraft or track the target within desired tracking accuracy. For these situations as well as for zero disturbance torque, the relationships required for designing an IPFM controller, following Ref. 2, are presented in Table 2.

Multiaxis Tracking Controller

Figure 3 depicts a three-axis IPFM controller for flexible spacecraft for target tracking. The six translational and rotational rigid modes are governed by

$$m\ddot{\boldsymbol{R}}_0 = \boldsymbol{F}_c \qquad \boldsymbol{I}\dot{\boldsymbol{\Omega}}_0 = \boldsymbol{T}_c \qquad (10)$$

where m = mass and $\boldsymbol{I}$ = 3 × 3 the central inertia dyadic of the vehicle; $\boldsymbol{R}_0$ = 3 × 1 rigid translation vector of the spacecraft mass center, measured from its nominal orbit and produced by the jet force $\boldsymbol{F}_c$ passing through the vehicle mass center; $\boldsymbol{\Omega}_0$ = 3 × 1 rigid, inertial angular velocity of the spacecraft; and $\boldsymbol{T}_c$ = 3 × 1 the control torque vector produced by the jets, about the spacecraft principle axes. In the rotational equation, it is assumed that $\boldsymbol{\Omega}_0$ is sufficiently small so that the gyric term $\boldsymbol{\Omega}_0 \times \boldsymbol{I}$. $\boldsymbol{\Omega}_0$ is negligible compared to $\boldsymbol{I}\dot{\boldsymbol{\Omega}}_0$ or $\boldsymbol{T}_c$. In Fig. 3, the Laplace transform of Eqs. (10) (with s as the Laplace variable) represents the rigid dynamics of the spacecraft. The translational deviation r_g of the gyro base from a nominal circular orbit, and the measured inertial angular rate $\boldsymbol{\omega}$ of the spacecraft, are obtained by augmenting $\boldsymbol{R}_0$ and $\boldsymbol{\Omega}_0$ with the contributions of the flexible modes as shown in Fig. 3 where $\chi_{\mu g}$ and $\boldsymbol{\Phi}_{\mu g}$ (μ = 1, 2, ...) are, respectively, the 3 × 1 translational and

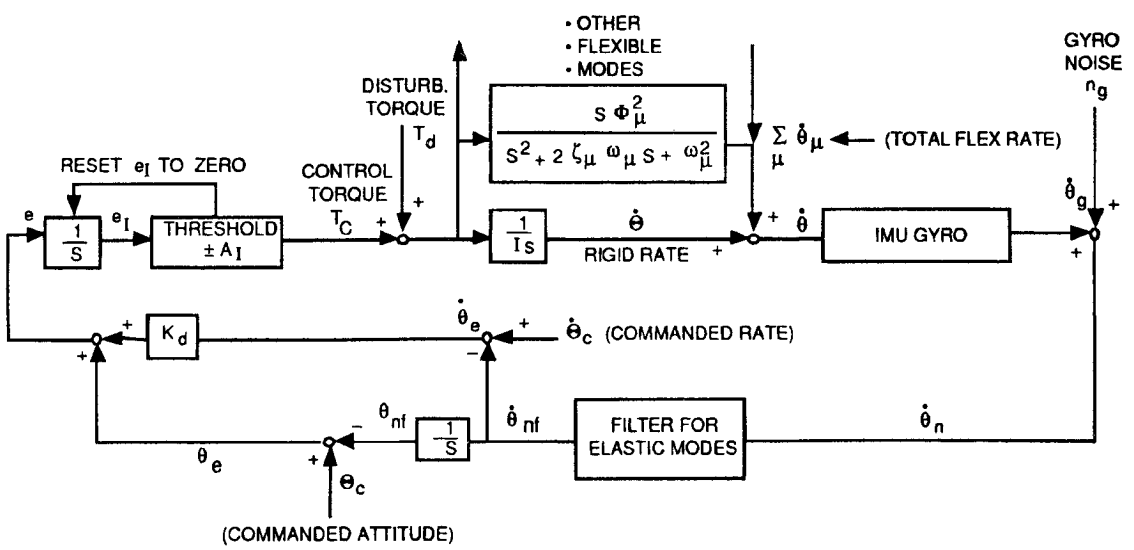

Fig. 2 Single-axis integral pulse frequency modulation reaction jet controller for flexible spacecraft.

Table 2 Determination of control parameters for rigid spacecraft[2,11]

Disturbance acceleration	$\alpha_d = \lvert T_d \rvert / I_y$ or commanded acceleration
Specified steady-state attitude offset under T_d	Θ_{ss}
Specified viscous damping coefficient of an equivalent linear proportional-plus-derivative controller	ζ_c
Minimum angular rate increment	$2\,\dot{\Theta}_L = \lvert T_c \rvert\, \tau_w / I_y$
Integral threshold	$A_I = 2\,\Theta_{SS}\,\dot{\Theta}_L/\alpha_d$
Parabolic limit cycle period under T_d	$\tau_{Ld} = 2\,\dot{\Theta}_L/\alpha_d = A_I/\Theta_{SS}$
Rate gain	$K_d = \zeta_c \sqrt{2A_I/\dot{\Theta}_L}$
Bandwidth of equivalent linear controller	$\omega_{bw} = 2\zeta_c / K_d$
Rectangular limit cycle attitude Θ_L (specified under no disturbance; dictated by preceding quantities when T_d is specified)	$\Theta_L = A_I/(2K_d)$
Rectangular, symmetric limit cycle period	$\tau_L = 4\,\Theta_L / \dot{\Theta}_L = A_I/(2\zeta_c^2\,\Theta_L) = K_d/\zeta_c^2$
Static saturation limits in attitude and rate	$\Theta_{sat} = A_I/\tau_w \quad \dot{\Theta}_{sat} = A_I/(K_d\tau_w)$

rotational modal coefficients at the gyro base. The question of how many modes to retain in the simulation is taken up in the next section. The vehicle elastic modes are governed by

$$\ddot{\eta}_\mu + 2\,\zeta_\mu\,\omega_\mu\,\dot{\eta}_\mu + \omega_\mu^2\,\eta_\mu = \boldsymbol{\chi}_{\mu J}^T \boldsymbol{F}_c \tag{11}$$

where ω_μ is the μth modal frequency and ζ_μ the associated modal damping coefficient; $\boldsymbol{\chi}_{\mu J}$ is the μth translational modal coefficient at the jet location.

The preceding quantity r_g is in the spacecraft-fixed frame. In the inertial frame, it is denoted r_g^I and is obtained by using the transformation matrix $\boldsymbol{C}_{ib}$. The system flexible modes do not possess momentum, and therefore the deviation of the spacecraft mass center from the nominal circular orbit is still $\boldsymbol{R}_0$. However, the spacecraft navigation system registers the quantity r_g, not $\boldsymbol{R}_0$. But the difference between the two is negligible compared to the nominal orbit radius r_s, and therefore the instantaneous radius of the spacecraft orbit could be regarded as the measured quantity $\boldsymbol{r}_s + r_g^I$, as shown in Fig. 3, to determine the instantaneous line-of-sight vector ℓ_I in the inertial frame. The quantity r_g (or $\boldsymbol{R}_0$), ignored in Sec. II, is included in Fig. 3 for precision tracking. Next, knowing the orbit inclination i and the instantaneous ascending node angle Ω_N (keeping nodal regression in mind), the line-of-sight vector ℓ_I is transformed to the local-vertical-local-horizontal circular orbit frame (Fig. 3): $\ell_c = \boldsymbol{C}_{ci}\,\ell_I$. To obtain the attitude error vector $\boldsymbol{\theta}_e$, the Euler angle rate vector $\dot{\boldsymbol{\theta}}$ is determined first from the gyro-measured inertial angular velocity vector $\boldsymbol{\omega}$. The current attitude is obtained next by integrating $\dot{\boldsymbol{\theta}}$ and knowing the previous $\boldsymbol{\theta}$. The small attitude error vector $\boldsymbol{\theta}_e$ is then: $\boldsymbol{\theta}_e = \boldsymbol{\theta}_c - \boldsymbol{\theta}$ where $\boldsymbol{\theta}_c = [\theta_{xc}\ \theta_{yc}\ 0]^T$. While this calculation of $\boldsymbol{\theta}_e$ is based on gyro measured $\boldsymbol{\omega}$, a more direct (closed-form) procedure is shown in Fig. 3 instead, based on the location of the target image in the focal plane. Using the last known attitude $\boldsymbol{\theta}$ of the spacecraft relative to the local orbit frame, the line-of-sight vector ℓ_c is transformed to ℓ_b in the spacecraft-fixed frame. Ideally, ℓ_b should be along the payload axis $-z_b$, but in reality the target image is off-centered by (ℓ_{xb}, ℓ_{yb}) in the focal plane $x_b y_b$. Therefore, if the spacecraft is commanded to rotate by the angles θ_{xe} and θ_{ye} (defined in Fig. 3) about the x_b- and y_b-axis, respectively, the target image will then be centered on the focal plane. Due to the focal plane noise and quantization, however, the measured errors will be $\theta_{eQ,x}$ and $\theta_{eQ,y}$ as shown in Fig. 3.

The advantage of this alternate scheme is that it does not use gyro measurements. During tracking, it is likely that the gyro measurements cannot be updated using stars and, therefore, depending on the tracking duration, the measurements could be grossly erroneous. The yaw attitude error, nonetheless, cannot be obtained from the focal plane measurements, and so it must be deduced from the yaw rate error ω_{ze} provided by the yaw gyro, as shown in Fig. 3. Recalling the linear relationships between the inertial rate errors (ω_{xe}, ω_{ye}, ω_{ze}) and small attitude errors (θ_{xe}, θ_{ye}, θ_{ze}), namely,

$$\omega_{xe} = \dot{\theta}_{xe} - \omega_0\,\theta_{ze} \tag{12a}$$

$$\omega_{ye} = \dot{\theta}_{ye} - \omega_0 \tag{12b}$$

$$\omega_{ze} = \dot{\theta}_{ze} + \omega_0\,\theta_{xe} \tag{12c}$$

the Euler rate error $\dot{\theta}_{ze}$ is determined from ω_{ze} using Eq. (12c), and then the yaw error θ_{ze} by integrating $\dot{\theta}_{ze}$ (Fig. 3). The rate errors ω_{xe} and ω_{ye}, on the other hand, are obtained by substituting the quantized attitude errors $\theta_{eQ,x}$ and $\theta_{eQ,y}$ and their derivatives in Eqs. (12a) and (12b). Finally, having determined the position and rate errors, the control torque about each axis is determined as before for a single axis; for illustration, the determination of the x-axis control torque T_{cx} is shown in Fig. 3. [I am indebted to Mr. Eugene Wells, Control Dynamics Co., Huntsville, Alabama for this idea.]

The IPFM controller discussed here can be used for large angle, multiaxis, attitude maneuvers as well, either from a given initial state to a fixed final state or for acquiring a moving target. For three-axis attitude maneuvers, the reference trajectories for attitude and rate for each axis can be constructed from the eigen-axis trajectory, following D'Amario and Stubbs,[12] and used in lieu of the target trajectory and the line-of-sight calculations in Fig. 3. Likewise, for acquiring a moving target, the iterative algorithm of Redding and Adams[11] can be employed to generate the position and rate command trajectories about the three axes.

IV. Spacecraft Flexibility Considerations

The IPFM controller design procedure in Sec. III. is for a rigid spacecraft, but it is intended to be used on a flexible spacecraft. Therefore, flexibility concerns are addressed below.

Mode Selection

The attitude angle $\theta_\mu(t)$ contributed by the μth mode and introduced in Eq. (9) is governed by [cf. Eq. (11)]

$$\ddot{\theta}_\mu + 2\zeta_\mu\,\omega_\mu\,\dot{\theta}_\mu + \omega_\mu^2\,\theta_\mu = \Phi_\mu\,\Phi_{\mu,eq}\,T_c(t) \tag{13}$$

where $\Phi_{\mu,eq}$ is the equivalent μth modal slope at the thruster location, defined as follows. If a vehicle mode is antisymmetric, and if the thrusters residing in the bus produce a pure control torque T_c at the vehicle mass center, $\Phi_{\mu,eq}$ is then the modal slope Φ_μ at the thruster location. Otherwise, $\Phi_{\mu,eq}$ is related to the translational modal coefficients at the thruster location according to Eq. (18) given below. To select important

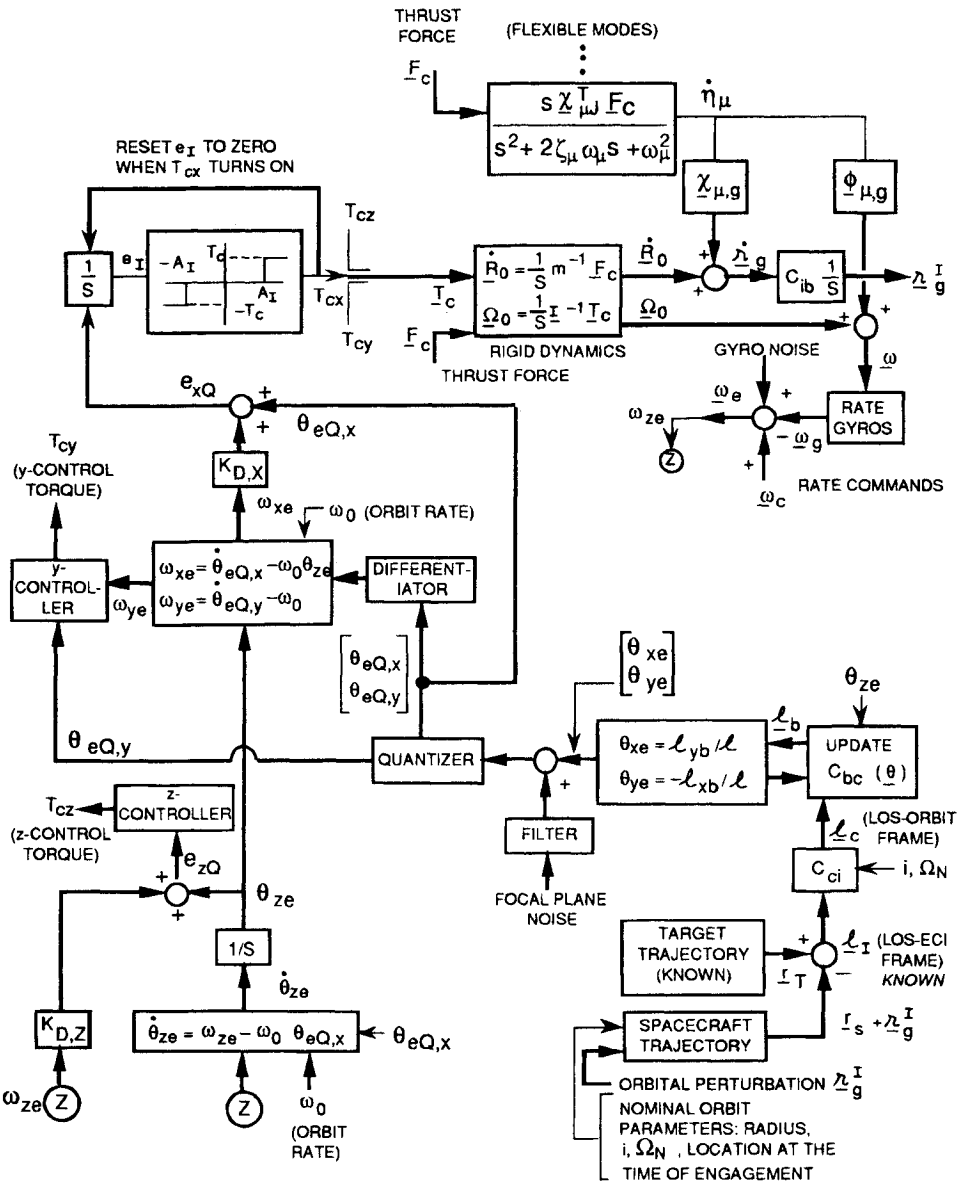

Fig. 3 IPFM controller for flexible spacecraft: multiaxis tracking.

elastic modes from a large number of them in a NASTRAN model, there are well-known metrics that quantify the importance of each mode. However, these metrics signify a long-term, steady-state modal response, not relevant to jet controllers. The spontaneous response of a mode is more relevant now, because it reveals immediate effects of thruster firings. The changes in the amplitudes of the modal rate $\dot{\theta}_\mu(t)$ and the mode θ_μ, denoted $\Delta\theta_\mu$, and $\Delta\theta_\mu$, respectively, arising from the minimum impulse bit $T_c\tau_w$, are:

$$\Delta\dot{\theta}_\mu = \Phi_\mu \Phi_{\mu\, eq} T_c \tau_w, \qquad \Delta\theta_\mu = \Phi_\mu \Phi_{\mu,\, eq} T_c \tau_w/\omega_\mu \quad (14)$$

Assuming $T_c \tau_w$ to be unity, the modes can be selected on the basis of Eq. (14). Unlike the steady-state metrics in the literature, $\Delta\theta_\mu$ and $\Delta\dot{\theta}_\mu$ are independent of the damping coefficient ζ_μ, for now we focus on a quarter or one-half modal period, following the impulse, and in this duration the damping has an insignificant influence on the modal response.

Interference of Modes in Controller Operation

Describing function and Lyapunov technique apart, it seems that for a reaction jet control system to be effective on a flexible spacecraft, the changes $\Delta\dot{\theta}_\mu$ ($\mu = 1, 2, \ldots$) should be

$$\Delta\dot{\theta}_\mu \ll 2\dot{\Theta}_L \quad (15)$$

The condition (15) will be satisfied if the ratio of the moment of inertia I_f of the flexible parts to the moment of inertia I_r of the rigid parts, both at the vehicle mass center and about the axis under consideration, is[9]

$$I_f / I_r \ll 1 \quad (16)$$

Whereas the conditions (15) and (16) consider a steady-state limit cycle regime, the excessive excitation of elastic modes during transients, wherein the reaction jets are away from the limit cycling, will be avoided if the equivalent linear controller bandwidth ω_{bw}, Table 2, is a decade smaller than a critical modal frequency ω_μ: $\omega_{bw} \ll \omega_\mu$.

Instability Due to Symmetric Elastic Modes: Linear Analysis

When the mass distribution of a spacecraft is symmetric, the attitude motion of its bus interacts with antisymmetric vehicle elastic modes only. However, for a spacecraft with two solar arrays with a z-offset, when the arrays are in the pitch-yaw (yz) plane, symmetric vehicle elastic modes—transverse bending, for instance—induce a pitch motion. As a result, any arbitrary

thruster pair that produces a y-torque is not acceptable, lest it produce instability despite the colocation of the thrusters and the gyros residing in the central rigid body. The precise stability condition that applies now is derived below.

In the transient regime, a reaction jet controller is equivalent to a linear proportional-plus-derivative controller. It is well known that this linear controller does not destabilize a vehicle's flexible mode if the actuator and the sensor are colocated and if they are both of the same genre: a torque actuator paired with a gyro or an attitude sensor, and a force actuator paired with a linear displacement sensor; see Conclusion 3 of Gevarter.[7] Otherwise, the colocation does not guarantee stability of flexible modes. Mathematically, when a rectilinear force acts on a flexible mode of a spacecraft, the mode is governed by [cf. Eqs. (11) and (13)]

$$\ddot{\theta}_\mu + 2\zeta_\mu\omega_\mu\dot{\theta}_\mu + \omega_\mu^2\theta_\mu = \Phi_\mu \sum_j \chi_{\mu j}^T f_j \qquad (17)$$

where f_j is the force vector produced by the j-jet, Σ_j extends over the thrusters fired simultaneously to produce a torque about a certain axis, and the superscript T means the transpose. The vector f_j may be written in terms of the jet's direction cosine vector a_j, possibly different from a unit vector because of thruster canting: $f_j = a_j f$, where f is the scalar force produced by each j-jet, assuming that all jets firing simultaneously produce the same thrust f. We further assume that these jets produce a control torque T_c at the vehicle mass center; then, if ℓ_{eq} denotes the equivalent moment arm, the torque T_c will be given by $T_c = f\ell_{eq}$. The stability of the mode μ, then, requires (Gevarter[7]) that

$$\Phi_\mu \Phi_{\mu,eq} \triangleq \Phi_\mu \left\{\sum_j \chi_{\mu j}^T a_j\right\} \Big/ \ell_{eq} > 0 \qquad (18)$$

(where from the definition of $\Phi_{\mu,eq}$ is evident). If $\chi_{\mu\oplus}$ denotes modal translation of the point that represents the vehicle mass center, and if the thrusters and the attitude sensors both reside in the central rigid body, the condition (18) can be written as[9]

$$\Phi_\mu \chi_{\mu\oplus}^T \left\{\sum_j a_j\right\} \Big/ \ell_{eq} + \Phi_\mu^2 > 0 \qquad (19)$$

For antisymmetric modes, $\chi_{\mu\oplus}$ equals zero, and then the inequality (19) is automatically satisfied. Thus, when symmetric elastic modes interact with spacecraft attitude, those jet pairs should be selected that satisfy the requirement (19) the most for all critical elastic modes.

V. Numerical Results and Discussion

The control schemes discussed earlier are implemented on two spacecraft—one with two solar arrays with a z-offset, and the other with only one solar array. Using nonlinear digital simulations, controller performance was studied under varied circumstances but, due to space limitations, only some of the most revealing results are discussed below.

Multiaxis Tracking with One-Winged Spacecraft

Figure 4 illustrates segments of ground tracks of a spacecraft in a circular orbit and a target in a certain trajectory. The direction of the LOS vector from the spacecraft to the target varies with time, as displayed by the succession of arrows in Fig. 4, with time t as a parameter. It is clear from the figure that the target is out of the spacecraft orbit plane, so both in-track (pitch, θ_{yc}) and cross-track (roll, θ_{xc}) commands are required for tracking. These commands are illustrated in Fig. 5, obtained by simulating the commands in Table 1 based on the roll-pitch sequence for a payload facing the nadir initially. The actual roll (θ_x) and pitch (θ_y) angles are also shown in Fig. 5, obtained by simulating the multiaxis IPFM controller shown in Fig. 3.

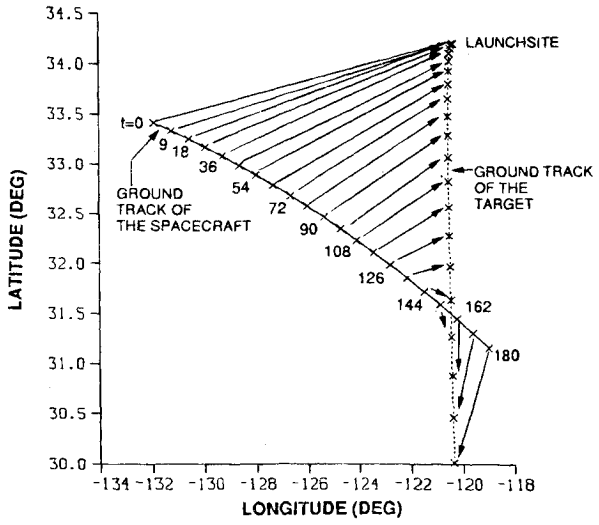

Fig. 4 Ground tracks of a spacecraft and a target on the rotating Earth.

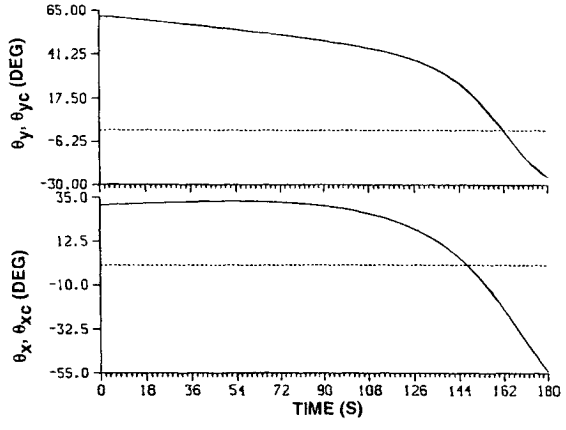

Fig. 5 Intrack (θ_{yc}) and crosstrack (θ_{xc}) Euler angle commands for tracking a moving object: spacecraft at 370 km altitude.

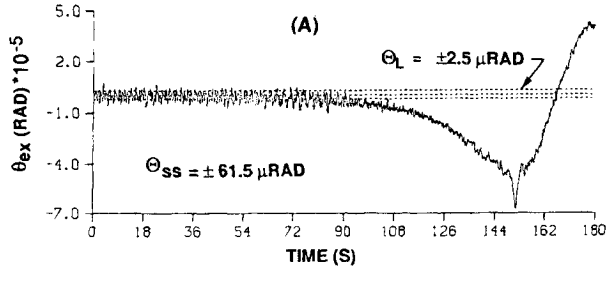

Fig. 6 Roll error during tracking a moving object with IPFM controllers.

The difference between the commanded and the actual angles, not visible in Fig. 5, is shown in Fig. 6 at a magnified scale for the roll axis. The profile of this tracking error resembles the commanded inertial angular acceleration profile about the same axis because the steady-state offset error Θ_{ss} equals $A_f\dot{\omega}_{xc}/(2\,\hat{\Theta}_L)$ (see Table 2) where $\dot{\omega}_{xc}$ is equivalent to α_d. Also, the controller is designed for the maximum commanded acceleration, leading to a permissible maximum offset Θ_{ss} equal to 61.5 μrad in Fig. 6. The controller is designed to be sufficiently fast so as to track the varying acceleration command profile in all axes, and therefore the instantaneous position errors θ_{xe} and θ_{ye} are very close to the respective, instantaneous offsets Θ_{ss} with slight jitter around them. Using single-axis dynamics, it can be shown that θ_{xe} varies between $\Theta_{ss} - \mu^2/(24\dot{\omega}_{xc})$ and Θ_{ss}

$+ \mu^2/(12\dot{\omega}_{xc})$, and therefore the peak-to-peak amplitude of the jitter around Θ_{ss} is $\mu^2/(8\dot{\omega}_{xc})$, inversely proportional to the commanded acceleration. This trend is observed in Fig. 6 where jitter amplitude is small in the high-acceleration regime after $t = 100$ s. In the low-acceleration regime, the jitter amplitude is not governed by this relationship; instead, it becomes equal to the peak-to-peak limit cycle amplitude $2\ \Theta_L$, observed in Fig. 6 in the low-acceleration regime before $t = 100$ s. The rate command ω_{xc} about the x-axis and the actual rate ω_x are shown in Fig. 7. The corresponding quantities about the y-axis have the same form, with slightly different magnitudes, and the rate command ω_{zc} is related to ω_{xc} as shown in Table 1; space limitations forbid the illustration of these quantities here, however. The spacecraft rate at $t = 0$ is set to be equal to the commanded rate, and therefore transients do not arise near $t = 0$ in Fig. 7. Furthermore, we observe from the numerical results that, whereas the commanded rates ω_{xc} and ω_{yc} are tracked closely, the rate ω_{zc} is not, particularly in the high-acceleration regime; this is intentional, as the yaw-axis controller need not be as tight as the roll and pitch controllers. The rate error ω_{xe} is shown at magnified scales in Fig. 8 for $160\ \text{s} \leq t \leq 180$ s, the duration in which the associated rate commands and the rate errors are the largest. The peak-to-peak jitter amplitude of the rate error is typically equal to $2\dot{\Theta}_L$, equal to 32 μrad/s. The control torque history about the roll, pitch, and yaw axes to effect multiaxis tracking is illustrated in Ref. 9. The results show that, when the roll and pitch track accelerations are much smaller than the control acceleration, the double-sided firings occur. Gradually, as the high track acceleration regime is approached, the one-sided firings take over.

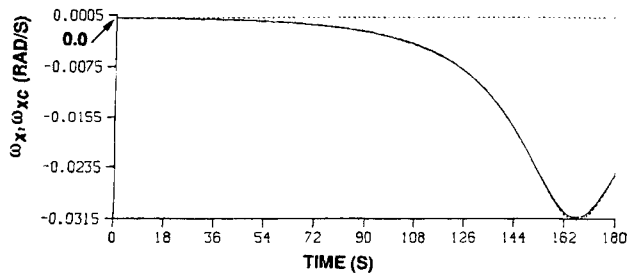

Fig. 7 Multiaxis tracking of a moving object: commanded inertial rate ω_{xc} and actual rate ω_x in spacecraft frame.

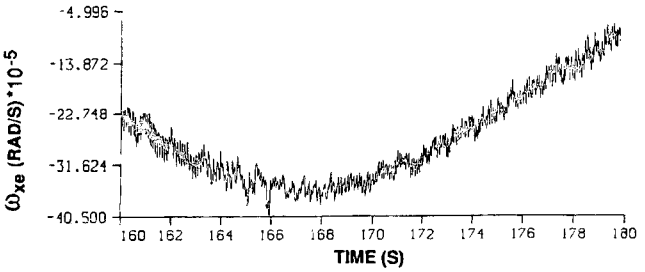

Fig. 8 Roll rate error, scales magnified: $160 \leq t \leq 180$ s.

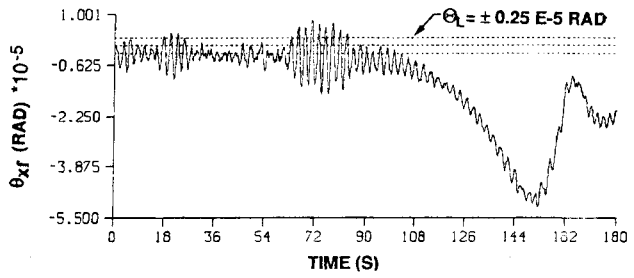

Fig. 9 Roll jitter caused by ten flexible modes.

The position error θ_{xe} shown earlier in Fig. 6 is made up of both rigid and flexible modes. The solar array at the time of tracking is tilted about the roll-axis and situated on the $+y$-side of the spacecraft. Its transverse bending (0.47 Hz, fundamental mode) induces roll motion; and the torsion and in-plane bending modes (1.38 and 1.77 Hz, fundamental modes) induce, respectively, pitch and yaw motion. The incremental attitude rates, Eq. (14), corresponding to these three fundamental modes, produced by the given minimum impulse bit of the thrusters, are

$$\Delta\dot{\theta}_x = 6.8\ \mu\text{rad/s} \qquad \Delta\dot{\theta}_y = 0.52\ \mu\text{rad/s}$$
$$\Delta\dot{\theta}_z = 55.9\ \mu\text{rad/s} \tag{20}$$

whereas the rigid limit cycle rates $\dot{\Theta}_L$ for the given vehicle moment of inertia about each axis are

$$\dot{\Theta}_{L,x} = 16.25\ \mu\text{rad/s} \qquad \dot{\Theta}_{L,y} = 16.25\ \mu\text{rad/s}$$
$$\dot{\Theta}_{L,z} = 40.7\ \mu\text{rad/s} \tag{21}$$

Clearly, the stability criterion (15) is satisfied for the x- and y-axis with considerable margin, and for the z-axis with little margin. For this reason, and also because the yaw pointing accuracy is not critical for tracking, the z-IPFM controller is not designed to be as tight as the x- and y-controllers as stated before. The most eventful, yet benign, control-structure interaction is seen in the roll-axis in Fig. 9, displaying the contribution θ_{xf} of ten flexible modes to the roll angle. The modal damping coefficient ζ_μ ($\mu = 1, 2, \ldots$.) is taken to be 0.0025 in the simulation. Most of θ_{xf} arises from the fundamental transverse bending mode (0.47 Hz). Because the track acceleration rises at a rate much slower than the 2.13 s period of this mode, the solar array bends quasistatically, with a maximum contribution of nearly 50 μrad to the roll angle (cf. Fig. 9).

Attitude Control During Stationkeeping: Spacecraft with Two Solar Arrays

Consider now a spacecraft with solar arrays on the $+y$- and $-y$-side in the pitch-yaw (yz) plane, hinged to the central bus with equal $-z$-offsets (zenith arrays). Because of this orientation, the fundamental symmetric elastic mode (a system mode, frequency 0.28 Hz) induces pitch motion (see Table 3). To ensure proper selection of the thrusters for y-control, the left side of the stability inequality (19) is calculated for different pairs of thrusters (Table 4) for both $+y$- and $-y$-torque, consid-

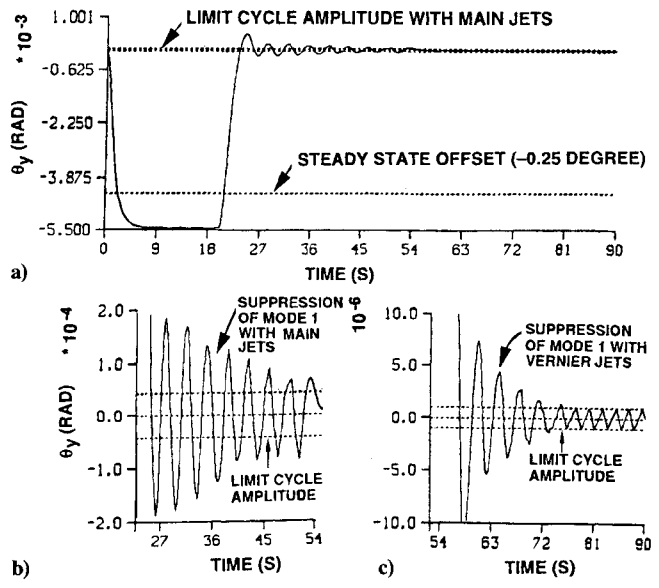

Fig. 10 y-axis control and vibration suppression during station keeping.

Table 3 IPFM controller and modal parameters for the generic flexible spacecraft

Axis	Fundamental interacting vehicle mode	Modal frequency, Hz	I_f/I_r	$\Delta\dot{\Theta}_\mu/2\dot{\Theta}_L$	Equivalent linear controller frequency, Hz	Θ_L, rad	Limit cycle period τ_L, s	Limit cycle period with disturbance τ_{Ld} s
x (roll)	In-plane antisymmetric bending	0.97	0.47	0.39	0.167	0.0324E-3	2.69	0.025
y (pitch)	Symmetric transverse bending	0.28	0.064	0.0636	0.18	0.04286E-3	2.52	0.025
z (yaw)	Antisymmetric transverse bending	0.40	1.7	1.166	0.009	28.4E-6	50.5	0.328

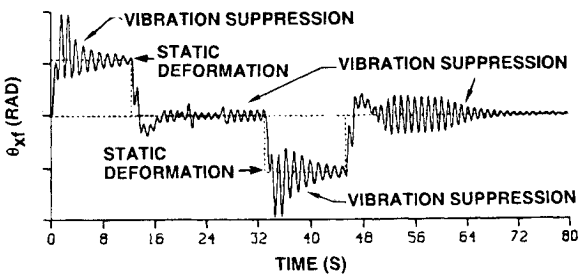

Fig. 11 Excitation and suppression of elastic mode 4 (0.97 Hz) during 90-deg slew.

Table 4 Modal gain for y-thrusters and stability characteristics

$+y$ torque pair	$-y$ torque pair	Symmetric transverse bending mode 1 gain	Stability property
6, 7	2, 3	0.182	Stable
1, 4	5, 8	−0.116	Unstable
1, 6	2, 5	0.033	Marginally stable

ering only the most dominating mode—mode 1. Evidently, the pairs (1, 4) and (5, 8) violate the condition (19) and therefore a controller using them will be unstable. Precisely this situation is inferred from the two encirclements of the critical point in the Nichols plots (not included here, for brevity) of a linear proportional-plus-derivative controller equivalent to the IFPM controller using the pairs (1, 4) and (5, 8). The equivalent proportional and derivative gains are $K_{p,eq} = I_y\,\omega_{bw}^2$, $K_{d,eq} = 2\,\zeta_c\,\omega_{bw}^2\,I_y$. Comparing the modal gains of the remaining pairs in Table 4, the pairs (6, 7) and (2, 3) are obviously the most stable. This is substantiated by the corresponding stable Nichols plot wherein we also observe that the gain/phase curves corresponding to the rigid spacecraft are stable regardless of the thruster pairs. These results were further confirmed by a time-domain simulation of the nonlinear IPFM controller for y-axis.

Using a single-axis flexible model, Figs. 10 and 11 illustrate the performance of the y-controller during 20 s of station-keeping disturbance and afterwards. During station keeping ($t \leq 20$ s), the pitch attitude (Fig. 10a) rises to the specified steady-state offset (actually, to a value slightly greater, because of 50 Hz sampling frequency instead of a higher one). When the station-keeping thrust is turned off at $t = 20$ s, the pitch attitude θ_y is gently brought to its natural limit cycle, amid some oscillations caused by the mode 1. The IPFM controller, however, linearly suppresses these oscillations as well, as shown at a magnified scale in Fig. 10b for main jets, active until $t = 52$ s, and at a still more magnified scale in Fig. 10c for vernier jets active afterwards. Beyond $t \approx 75$ s, the angle θ_y is essentially a rigid angle, exhibiting a limit cycle behavior. In this example, the IPFM controller suppresses mode 1 successfully because, as shown in Table 3, $I_f/I_r \approx \Delta\dot{\theta}_\mu/2\dot{\Theta}_L \approx 0.064 \ll 1$ for the y-axis.

As a side comment, the above smooth performance of the IPFM controller contrasts sharply with the jerky behavior of the pulse-width-pulse-frequency (PWPF) controller in Fig. 7, Ref. 5 under similar circumstances. The undesirable features of the latter controller are the significant oscillations of the position error around Θ_{ss} under a constant disturbance, and the limit cycle amplitude $2\Theta_L$ as much as Θ_{ss}. These features arise because the PWPF torque command, unlike the IPFM command, is governed by the instantaneous position and rate errors, not by their integrals.

The performance of the x-IPFM controller is similar to that of the y-controller. The ratios I_f/I_r and $\Delta\dot{\Theta}_\mu/2\dot{\Theta}_L$ satisfy the inequalities (15) and (16) (see Table 3) and therefore the fundamental antisymmetric in-plane bending modes, inducing roll, is suppressed by the controller. This is exhibited in Fig. 11, displaying the contribution of the mode 4 (0.97 Hz) to the roll motion during a 90-deg slew preceeding the station keeping. To execute the slew motion, the fuel/time optimal reference trajectories in attitude and attitude rate are used as command profiles. The smooth slewing performance (as an acquisition problem) is discussed and illustrated in detail in Ref. 9. To understand the vibration suppression during slew (Fig. 11), recall that in an open-loop system the first acceleration pulse excites the elastic modes to twice the static deformation. But here we observe that the IPFM controller stunts the oscillation from the beginning and suppresses it quickly to its static deformation level (it cannot be suppressed any further, with the thrusters residing in the spacecraft bus) and to very small rates. During coasting, thrusters are not fired, so the corresponding static deformation is zero and the jets now suppress the earlier static deformation to nearly zero amplitude. During deceleration phase and subsequently, the controller redisplays its vibration suppression ability. The coasting phase in the slew process not only reduces fuel consumption, it also presents a time interval to the controller during which the controller can suppress the rigid offset error in the slew angle of the spacecraft (such as 0.25 deg in Fig. 10a) and the positive static deformation θ_{xf} in Fig. 11; otherwise, the deceleration pulse immediately following the error will suddenly impose opposite rigid offset error and static deformation, accentuating the prior errors and usually destabilizing the spacecraft.

As for the yaw axis, Table 3 shows that the inequalities (15) and (16) are both violated, and therefore an instability owing to the mode 4 (0.4 Hz) is likely. The z-IPFM controller, designed by ignoring the flexibility, is indeed found to be unstable through a time-domain simulation of the flexible z-axis. In the frequency domain, though, this instability is foreshadowed but not apprehended by the Bode plot of an equivalent linear controller by indicating a gain of 15 dB at the modal frequency 0.4 Hz. This instability is eliminated by inserting a minimum-rise-time, low-pass filter, resulting in a controller that not only controls the spacecraft about the z-axis during slews and station keeping, but suppresses the mode 2 as well, albeit only slightly. The corresponding time domain and the frequency-domain results are displayed and discussed in Ref. 9.

VI. Concluding Remarks

The preceding results conclusively establish that the integral pulse frequency modulation (IPFM) reaction jet controllers are useful for multiaxis target tracking, spacecraft attitude control

under disturbances, single-axis slews, and vibration suppression. The problem has not been solved in its entirety, though; for instance, multiaxis acquisition of a moving target, in which case the final attitude and rate of the spacecraft are a function of the acquisition time, has yet to be considered, possibly using quarternions. Nevertheless, it can be stated with confidence that thrusters, when operated by the IPFM controllers, are viable alternatives to reaction wheels and control moment gyros for precision and low-jitter acquisition and tracking of moving targets by flexible spacecraft. If the inertia ratio of the flexible to the rigid portions of the spacecraft is fairly below unity, the IPFM controller suppresses even the vibrations of structural modes because of these unique attributes: integration of position and rate errors, constant pulsewidth, and modulation of thruster firing frequency.

Acknowledgment

The work reported in this paper was performed over several years. I am grateful to my dear colleagues and kind friends Mr. A. Cormack III and Mr. L. A. Schmidt, Attitude Control Lead Engineers, for giving me valuable opportunities, on different occasions, to develop the preceding control systems, and to Mr. W. M. Logan, Program Manager, for funding these efforts.

References

[1] Hablani, H. B., "Design of a Payload Pointing Control System for Tracking Moving Objects," *Journal of Guidance, Control, and Dynamics*, Vol. 12, No. 3, 1989, pp. 365–374; also *Proceedings of the AIAA Guidance, Navigation, and Control Conference* (Monterey, CA), AIAA, Washington, DC, August 1987, pp. 1481–1494.

[2] Farrenkopf, R. L., Sabroff, A. E., and Wheeler, P. C., "Integral Pulse Frequency On-Off Control," *Guidance and Control II*, edited by R. C. Langford and C. J. Mundo, Vol. 13, Progress in Astronautics and Aeronautics, AIAA, New York, 1964, pp. 185–216.

[3] Abdel-Rahman, T. M. M., *The Effects of Structural Flexibility on the Nonlinear Attitude Control of Spacecraft*, Inst. for Aerospace Studies, Univ. of Toronto Inst. for Aerospace Studies, Rep. No. 222, Dec. 1977.

[4] Millar, R. A., and Vigneron, F. R., "Attitude Stability of a Pseudorate Jet-Controlled Flexible Spacecraft," *Journal of Guidance and Control*, Vol. 2, No. 2, 1979, pp. 111–118.

[5] Wie, B., and Plescia, C. T., "Attitude Stabilization of Flexible Spacecraft During Stationkeeping Maneuvers," *Journal of Guidance, Control, and Dynamics*, Vol. 7, No. 4, 1984, pp. 430–436.

[6] Anthony, T. C., Wie, B., and Carroll, S., "Pulse Modulated Control Synthesis for a Flexible Spacecraft," *Proceedings of the AIAA Guidance, Navigation, and Control Conference* (Boston, MA), AIAA, Washington, DC, 1989, pp. 65–76.

[7] Gevarter, W. B., "Basic Relations for Control of Flexible Vehicles," *AIAA Journal*, Vol. 8, No. 4, 1970, pp. 666–672.

[8] Blakelock, J .H., *Automatic Control of Aircraft and Missiles*, John Wiley and Sons, New York, 1991, Sec. 11.9, pp. 429–436.

[9] Hablani, H. B., "Target Acquisition, Tracking, Spacecraft Attitude Control, and Vibration Suppression with IPFM Reaction Jet Controllers," *Proceedings of the AIAA Guidance, Navigation and Control Conference* (Hilton Head, SC), AIAA, Washington, DC, 1992, pp. 1118–1137.

[10] Bernussou, J., "Satellite Attitude Control by Reaction Jet Frequency Modulation," *Journal of Spacecraft and Rockets*, Vol. 10, No. 1, 1973, pp. 52–55.

[11] Redding, D. C., and Adams, N. J., "Optimized-Rotation-Axis Attitude Maneuver Controller for the Space Shuttle Orbiter," *Journal of Guidance, Control, and Dynamics*, Vol. 10, No. 1, 1987, pp. 4–13.

[12] D'Amario, L. A., and Stubbs, G. S., "New Single-Rotation-Axis Autopilot for Rapid Spacecraft Attitude Maneuver," *Journal of Guidance and Control*, Vol. 2, No. 4, 1979, pp. 339–346.